RICE UNIVERSITY

Imaging the Pacific Plate and Transition Zone beneath Eastern Asia with Receiver Functions

by

Xinling Wang

A THESIS SUBMITTED
IN PARTIAL FULFILLMENT OF THE
REQUIREMENTS FOR THE DEGREE

Master of Science

APPROVED, THESIS COMMITTEE

Fenglin Niu,
Professor, Earth Science

Alan Levander
Professor, Earth Science

Julia K. Morgan
Professor, Earth Science

HOUSTON, TEXAS

NOVEMBER, 2011

Abstract

Imaging the Pacific Plate and transition zone beneath eastern Asia with receiver functions

by

Xinling Wang

In this thesis, I applied receiver function techniques to the data recorded by national and regional broadband seismic networks of the China Earthquake Administration to image the mantle transition-zone structure beneath eastern Asia. I analyzed a total of 37427 receiver-function data. Significant topography on both the 410-km and 660-km discontinuities was clearly imaged in the 3D volume of CCP (common-conversion-point) stacked images that cover an area of 102.5°-122.5°E and 22.0°-42.°N. 3D crustal and mantle velocity models were used in computing the Ps time move-outs to better image the absolute depths of the two discontinuities. I found that the 660-km discontinuity is depressed up to 25 km along the east coast of China, indicating the presence of the subducted Pacific slab in the region. More interestingly, a double 660-km was observed beneath the Yellow Sea, which was not seen from the 410-km discontinuity. I found a strong and localized anomaly beneath the Quaternary Datong volcano located at the northeastern edge of the Ordos plateau in north China. The 410-km is depressed by as much as 15 km beneath the volcano. If the amount of the depression is caused by un-modeled low velocity anomaly in the upper mantle, it requires either a strong (4-8%) localized low velocity anomaly near the lithosphere-asthenosphere boundary or ~1.5% low

velocity column across the entire upper mantle above the 410-km. The later could suggest a deep origin of the Datong volcano, although it was usually attributed to edge driven convection by most of the literatures.

Acknowledgments

Foremost, I would like to express my sincere gratitude to my advisor, Prof. Fenglin Niu, for his continuous support and close guidance of my research last two years. He provided good academic atmosphere and helped me making fast progress on my research projects. I learned a lot from Fenglin, his enthusiasm and immense knowledge in science and life. I could not have imagined having a better advisor and mentor for my master study. It is a great pity for me that I cannot finish my PhD study with him.

Besides my advisor, I would like to thank the rest of my thesis committee: Prof. Alan Levander and Prof. Julia K. Morgan for their encouragement, insight comments and instructive suggestions.

I am indebted to my many student colleagues for providing a stimulating and fun environment in which to learn and grow. I am especially grateful to Kaijian Liu, Yongbo Zhai, Xin Cheng, Yang He, Huafeng Liu, Jeniffer Masy, Sally Thurner, Jennifer Mackenzie, and Ya Sun. Yongbo and Kaijian is particularly helpful making me fast settle down and know many new friends at Houston.

I would like to thank my parents, sisters and brother for their love and unconditional support.

Contents

List of Figures

List of Equations

Chapter 1

Introduction

The structure and tectonics of eastern Asia are affected by the interactions of five tectonic plates: the Eurasian, Pacific, Okhotsk, Philippine Sea and Indian plates (Figure 1.1) (Huang and Zhao, 2006). In the southwest, India-Asia collision leads to the shorting and elevation of the Tibetan plateau, causing high and great mountain ranges such as the Himalaya, Pamirs, and the Hindu-Kush Mountains (Zhao et al., 2011). In the east, the Pacific and Philippine Sea plates are subudcting beneath Okhotsk and east Eurasian plates, causing the western Pacific islands arcs, marginal seas, and continental rift zones. Pacific plate, roughly 5000 km subducted under Japan during the last 50 Ma, extends down to 600 km depth near the eastern edge of China and is sharply deflected to horizontal and penetrates into the transition zone when it hits the bottom of upper mantle (Figure 1.2) (Huang and Zhao, 2006; Fukao et al, 2009). The horizontal slab stretches over distance of 800 to 1000 km in the transition zone along 660 km discontinuity. There are many intriguing geological

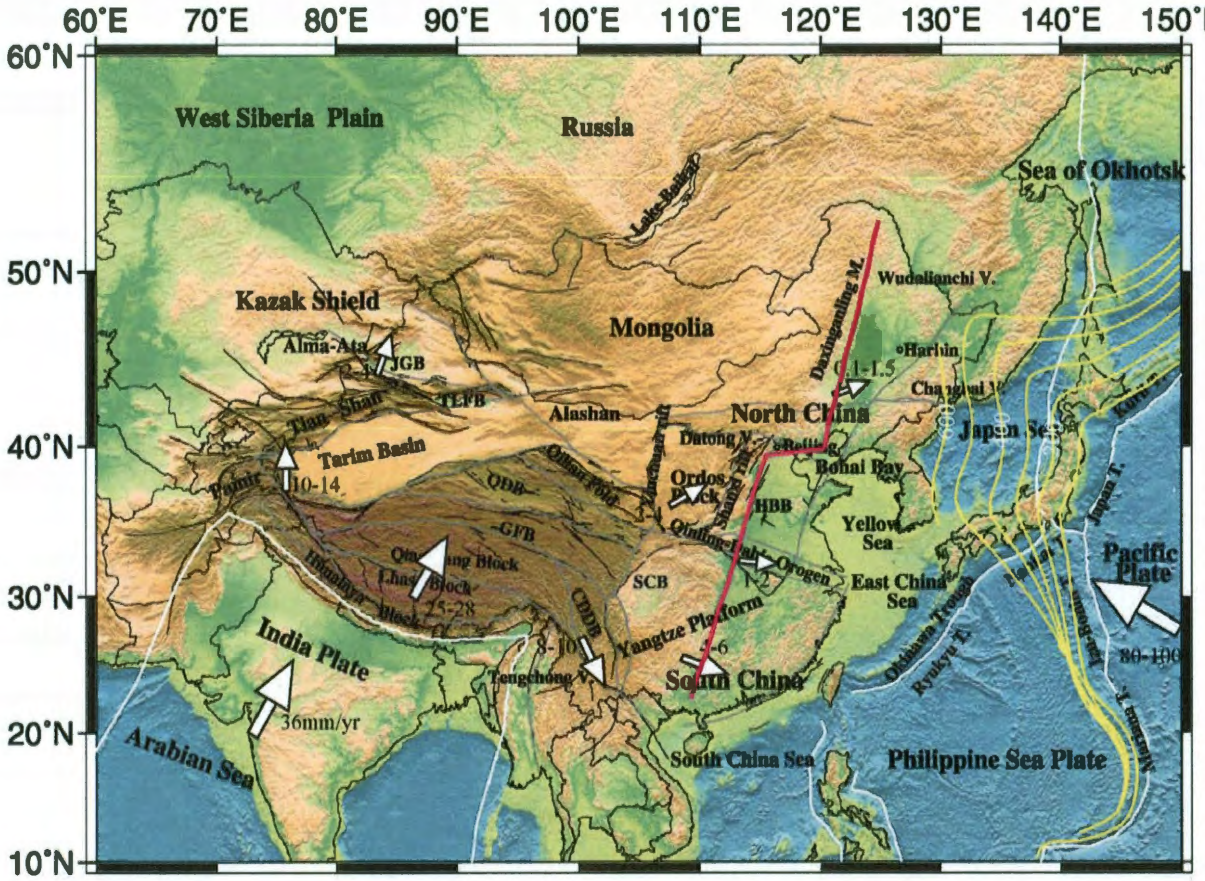

Figure 1.1 Map showing the major geological features of the study area. White curved lines show the plate boundaries. Grey thin curved lines show the large fault zones and/or tectonic block boundaries in mainland China. White arrows illustrate the plate motion directions and velocities basing on GPS results. Red line is North South Gravity Lineament. The slab depth contour is shown by yellow lines. Abbreviations are Jungger Basin (JGB), Qaidam Basin (QDB), Sichuan Basin (SCB), Tulufan Basin (TLFB), Songpan Ganzi Fold Belt (SGFB), and Chuandian Diamond Block (CDDB).

and geophysical features, which are related to the process Pacific slab subducting (Figure 1.3) (Zhao et al, 2011), such as the origin of the intraplate volcanoes, the structure and fate of stagnant slabs, deep earthquakes, lithospheric thinning and reactivation of the North China Craton, and the origin of intracontinental rift zones, etc. One of fundamental issues for understanding the dynamic and evolution of the Earth's mantle is what processes occur when subducting slabs interact with the transition zone. Therefore, East Asia, extending from northeast to south China, is an ideal natural laboratory to study characters of the transition zone and interaction with subducting slabs.

The interaction of these plates has resulted in a unique topographic contrast between eastern and western China (Figure 1.1). The two regions are bounded by a ~100 km wide, NNE trending lineament known as the North South Gravity Lineament (NSGL). The prolonged collisions in the west have shaped the region west of the NSGL into plateaus and highlands with elevations of ~500-6000 m above the sea level. On the other hand, the rollback of the Pacific slab appeared to play a dominant role in shaping the area located at the east of the NSGL, which is comprised primarily of extensional basins with an altitude <200 m. Besides the topographic contrast, the two regions also have very different seismicity, gravity anomaly, heat flow, crustal and lithosphere structure. Although the geological and structural contrast between eastern and western China can be roughly explained by the interaction between the Eurasian, Pacific and Indian plates, it is still unclear whether this contrast is caused dominantly by a crustal or a mantle process, or a combination of both. Based on a high-resolution image of the P-wave velocity

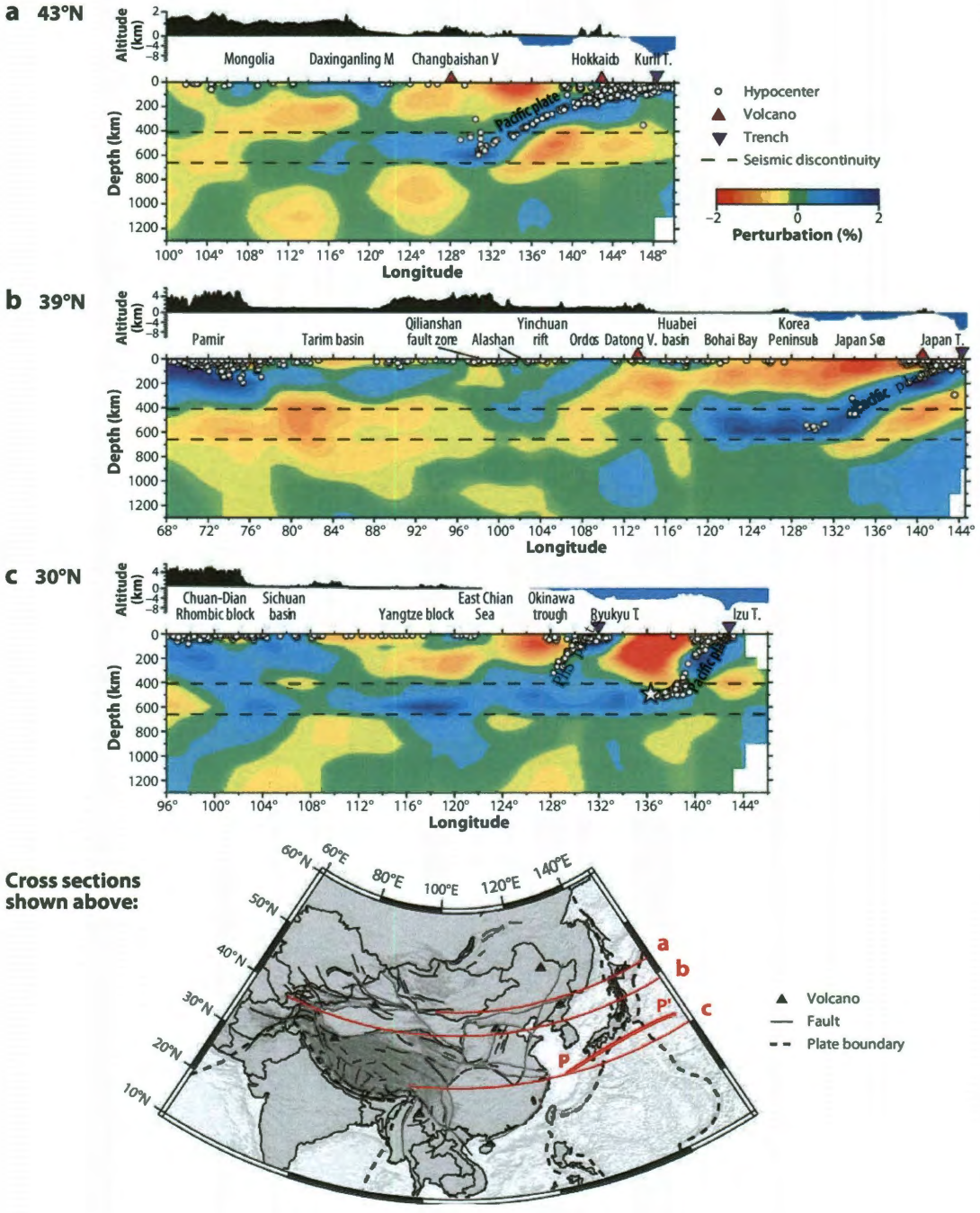

Figure 1.2 East-west vertical cross sections of P-wave velocity perturbations along latitudes 43◦, 39◦, and 30◦, where the horizontal slab extends over a distance of 800 to 1000 km above the 660 km discontinuity. Modified from Huang and Zhao (2006).

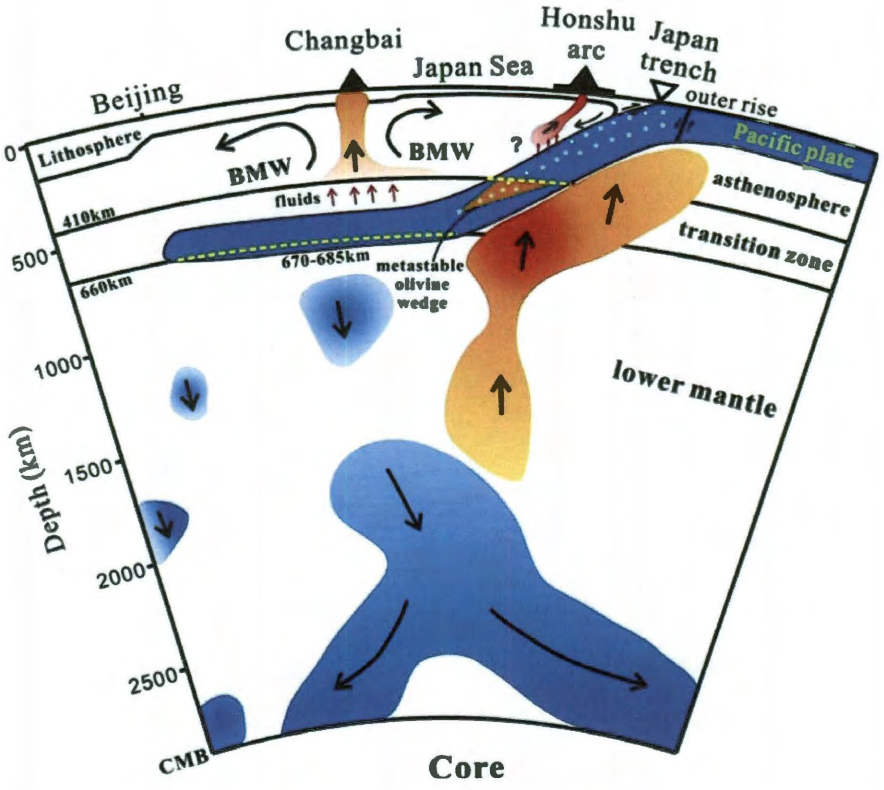

Figure 1.3 A cartoon summarizes the main features of mantle structure and dynamics under eastern Asia, including subducting Pacific plate and stagnant slabs in the transition zone, stagnant slabs sinking into lower mantle, and Changbai Shan volcano formation because of bigger mantle wedge, et al (Zhao, 2011).

structure beneath China, Huang and Zhao (2006) observed a good correlation between the locations of the NSGL and the western front of the subducted Pacific slab in the transition zone. They further suggested that the subhorizontally lying Pacific plate at the base of the upper mantle forms a big mantle wedge that defines the extensional area at earth's surface. This correlation, however, is not so clear in the tomographic images of Li and van der Hilst (2010).

While seismic tomography offers a direct way to map a descending slab with a high seismic velocity, receiver function data provides an indirect approach to image a subducting slab when it enters the mantle transition zone (e.g., Niu et al., 2005; Huang et al., 2010). The mantle transition zone is the layer between two discontinuities in seismic wave speed that lie at depths of approximately 410-km and 660-km (Anderson, 1989) (Figure 1.4). The 410-km and 660-km seismic discontinuities are associated with the temperature-sensitive phase transitions from olivine to wadsleyite (Katsura and Ito, 1989) and from ringwoodite to perovskite plus magnesiowustite (Ito and Takahashi, 1989), respectively. The latter is also known as the post-spinel transformation. Because the two phase-transitions have positive and negative Clapeyron slopes, respectively, a decrease in temperature results in a decrease in the depth to the 410-km discontinuity and an increase in the depth to the 660-km discontinuity. Lateral variations in the transition-zone thickness, as well as variations in the depths of the two discontinuities thus can be used to indirectly map out a descending slab and physical and chemical characters of the transition zone. While seismic tomography offers a direct way to map a descending slab with a high seismic velocity (e.g., Fukao,

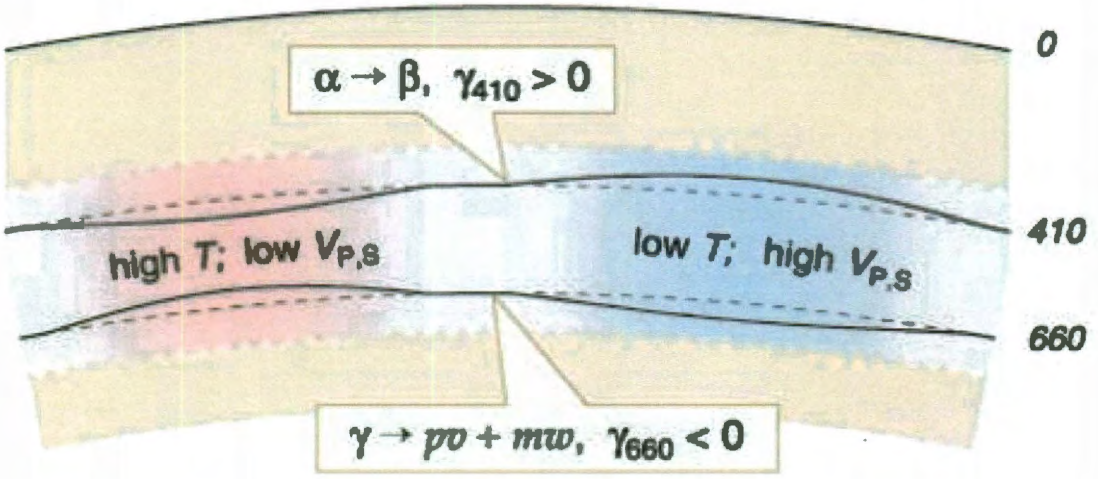

Figure 1.4 Schematic depiction of the transition zone in an olivine-dominant mantle. The α→β and γ→*pv* + *mw* phase transformations give rise to the 410- and 660-km discontinuities, and the effective Clapeyron slopes γ_{410} and γ_{660} have opposite signs. Absent lateral variations in composition, relatively low temperatures (*T*) cause thickening of the TZ and increase in seismic velocities (V_P, V_S); high temperatures cause thinning of the TZ and decrease in $V_{P,S}$ (Lebedv, et al, 2002).

et al, 2009; Huang and Zhao, 2006; Li, et al, 2010), one difficult with interpretation of seismic tomography images is that there still significant issues of resolution. Receiver function analysis, utilizing P to S conversions from teleseismic P waves, provides an indirect approach to image a subducting slab when it enters the mantle transition zone (e.g., Niu et al, 2005). Receiver function methods are sensitive to discontinuities in seismic properties. Numerous recent studies demonstrate that this approach is highly complementary to P and S wave tomography. Many previous researchers (e. g. Li et al, 1998; Shen et al, 1998; Ai et al, 2007; Chen et al, 2009; etc) presented their study results around this region using different receiver function techniques, but since the lack of data, they did not provide high resolution the transition zone images of the whole region beneath northeast and south China. The recent rapid growth of broadband seismic observation in China has opened a new era for imaging the crustal and mantle structure and dynamics beneath China. In this study, I took advantage of the recently dataset collected by the national and regional seismic networks operated by the China Earthquake Administration (CEA) and IRIS (Fig. 1.5). I applied receiver function techniques to the data to image the mantle transition-zone structure beneath eastern Asia. Our primary goal is to seek better understanding the structure in detail of mantle transition zone beneath eastern and central China.

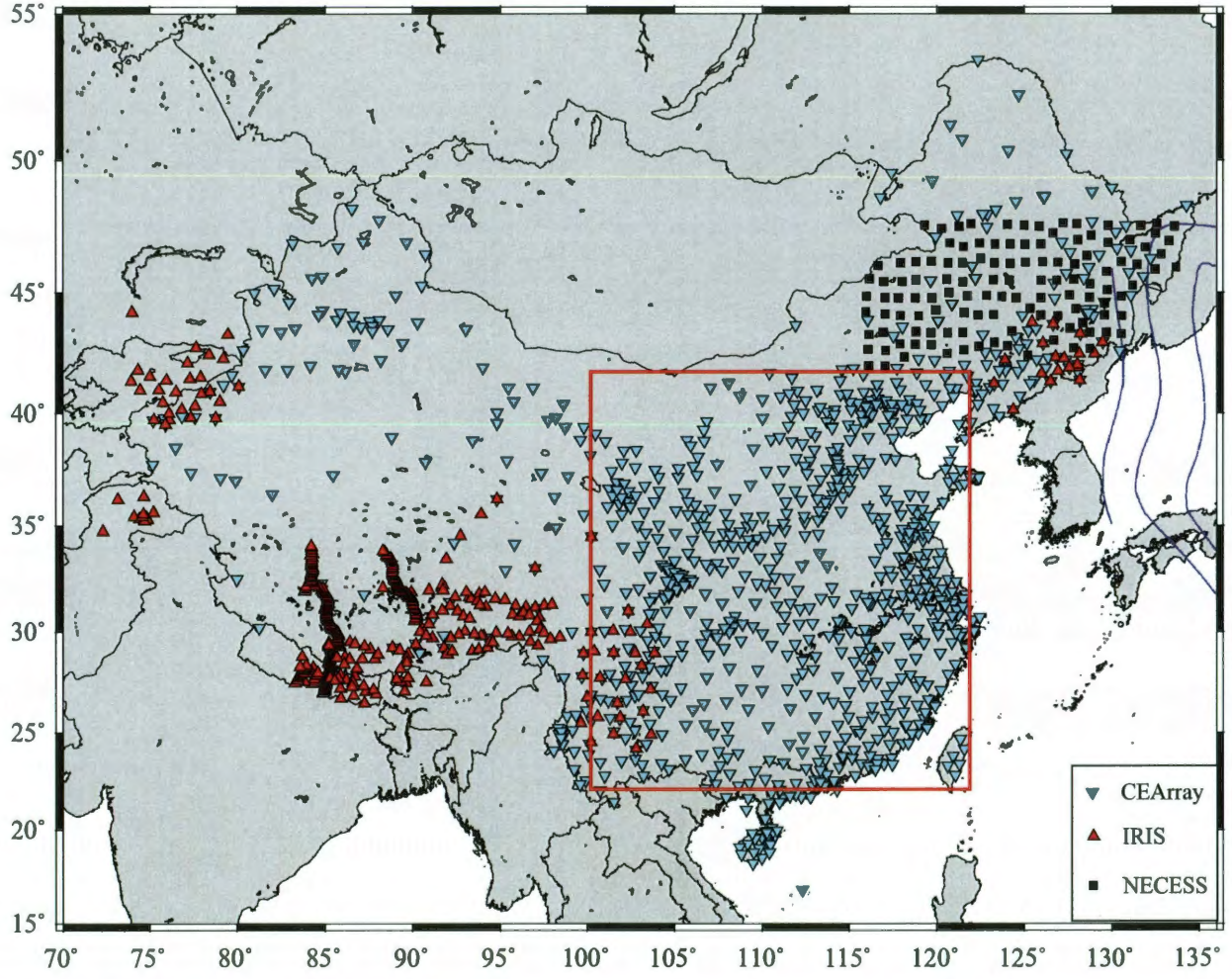

Figure 1.5 Station distribution of CEArray, NECESS and other arrays operated by IRIS in China. The red rectangular region shows the location of the study area.

Chapter 2

Data

The new CEA seismic network, completed in early 2007, consists of a backbone national seismograph network, 31 provincial networks, and several small aperture arrays with more than 1000 stations including 850+ broadband stations (Zheng et al, 2009) (Figure 1.5). The 1000+ stations formed a large 2D areal array with an aperture ~6700 km from east to west and ~3500 km from north to south. For the remainder of this thesis, I will refer to these stations as the CEArray. Station spacing varies drastically from location to location. I calculated the number of stations in a circular bin with a radius of 1° at a meshed grid of 1°×1° and found that the numbers vary from 0 to 53 (Figure 2.1). The eastern and central China (red box in Figure 2.1) is relatively well covered by stations, with an inter-station spacing of ~30-100 km, allowing the use of modern array techniques, such as common-conversion-point (CCP) gathering and pre-stack depth migration to image the upper mantle and transition zone structure beneath the array. Figure 2.2 illustrates

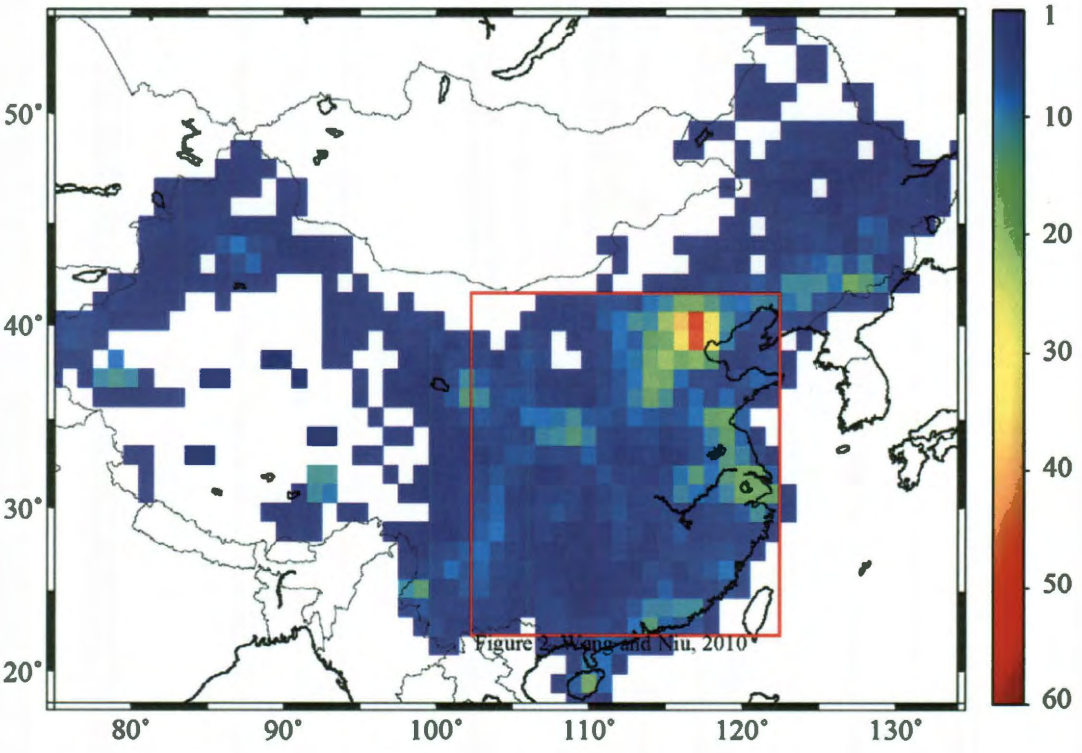

Figure 2.1 Map showing the density of seismic station across China. Station density is calculated from the number of stations located in a circular cap with a radius of 1 degree. A station density of 9 and 25 roughly corresponds to an inter-station spacing of 100 and 50 km, respectively. Red box indicates the study area.

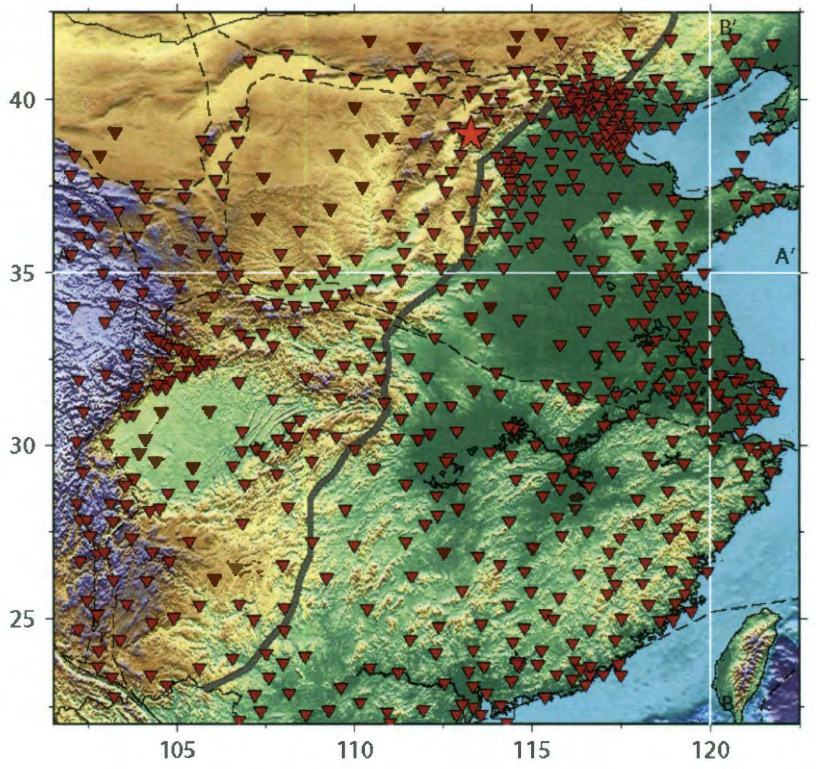

Figure 2.2 Map showing the broadband seismic stations (red triangles) of the CEArray. The thick grey line and the red star indicate the North South Gravity Lineament (NSGL), and the Quaternary Datong volcano, respectively. The two white lines, AA' and BB', show the locations of the two profiles shown in chapter 3.

station distribution in the research region.

I visually examined all the earthquakes with magnitude greater than 5.0 and in the epicentral distance of 30°–90° recorded between July of 2007 and early August of 2008. I chose 124 earthquakes with good signal-to-noise ratio (SNR). These earthquakes provide a reasonably good distance and azimuth coverage (Figure 2.3), although a large portion of the events are clustered in the western Pacific and the Java trench with a back azimuth between 30° and 210°.

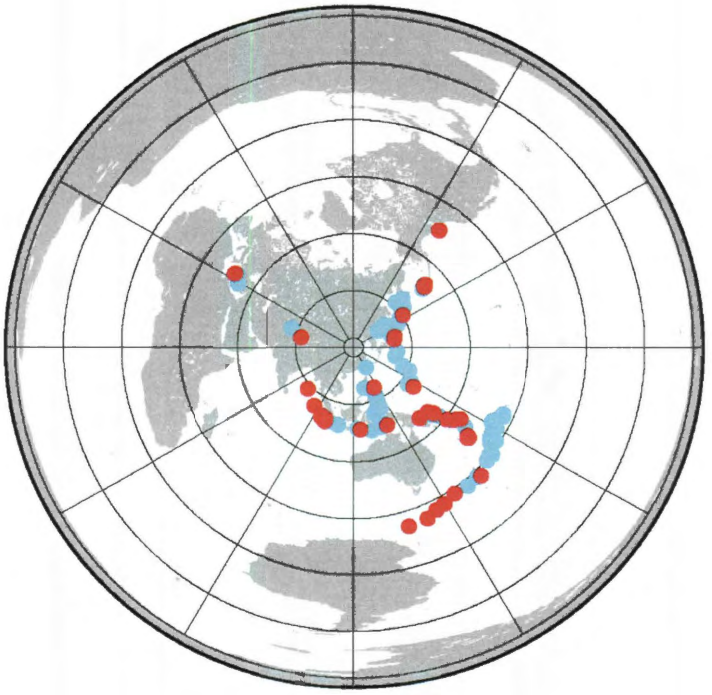

Figure 2.3 124 teleseismic event locations used in this study. (Red circles <50 km, cyan circles > 50 km).

Chapter 3

Methods

Receiver function analysis, utilizing P to S conversions from teleseismic P waves, has become a standard and popular technique to constrain crustal and upper mantle velocity discontinuities under a seismic station. Receiver function methods are sensitive to discontinuities in seismic properties. Telesismic body waveforms recorded at a three-component seismic station contain a wealth of information on the earthquake source, the earth structure in the vicinity of both source and the receiver, and mantle propagation effects (Figure 3.1). The resulting receiver function is obtained by removing the effects of source and mantle path. The basic aspect of this method is that a few percent of the incident P wave energy from teleseismic events at significant and relatively sharp velocity discontinuities in the crust and upper mantle will be converted to S wave (Ps), and arrive at the station within the P wave coda directly after the direct P wave (Figure 3.2). Ps converted waves are best observed at epicentral distances between 30° and 90° and are

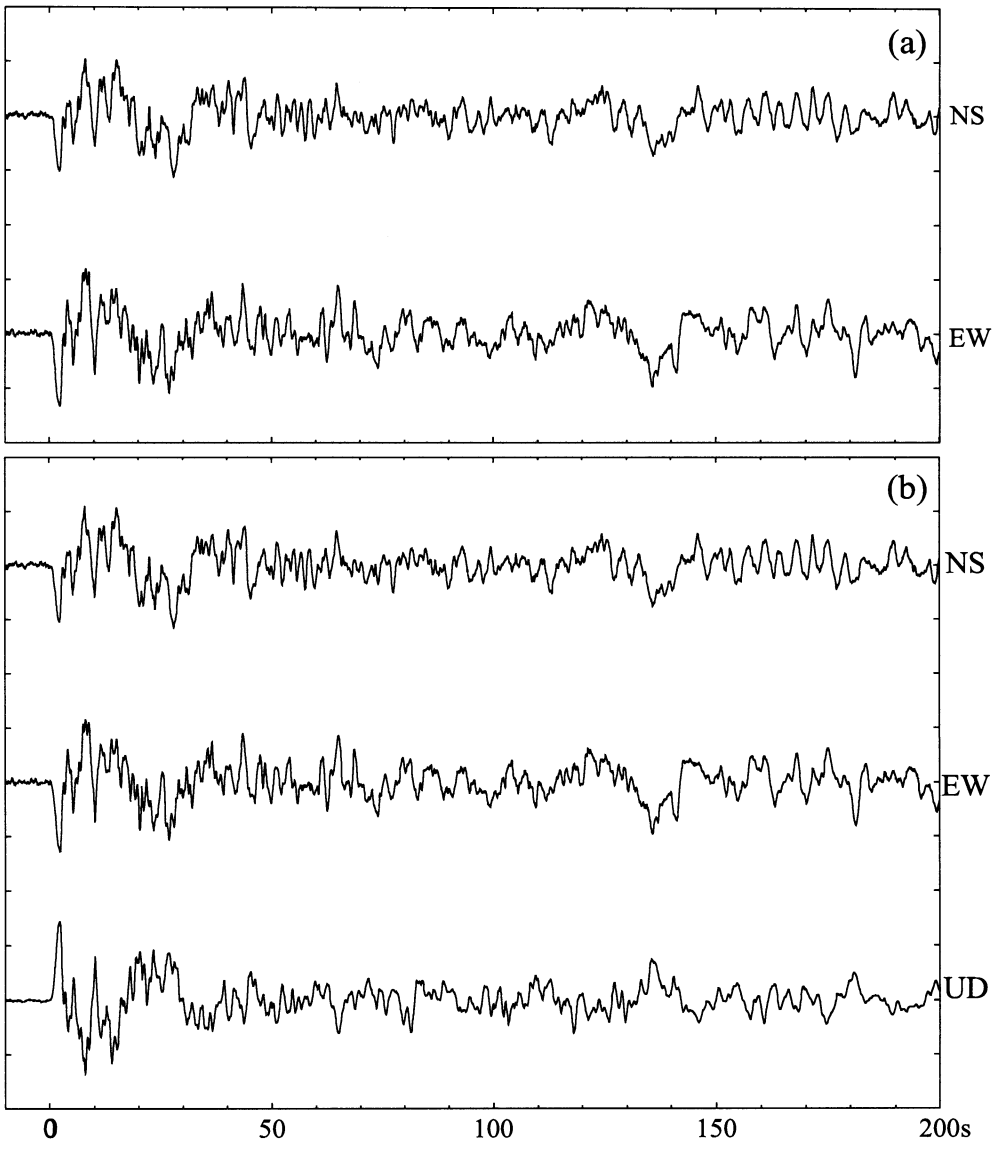

Figure 3.1 (a) shows the NS and EW components of seismic waves without correction. (b) illustrates three components of seismic waves with orientation correction.

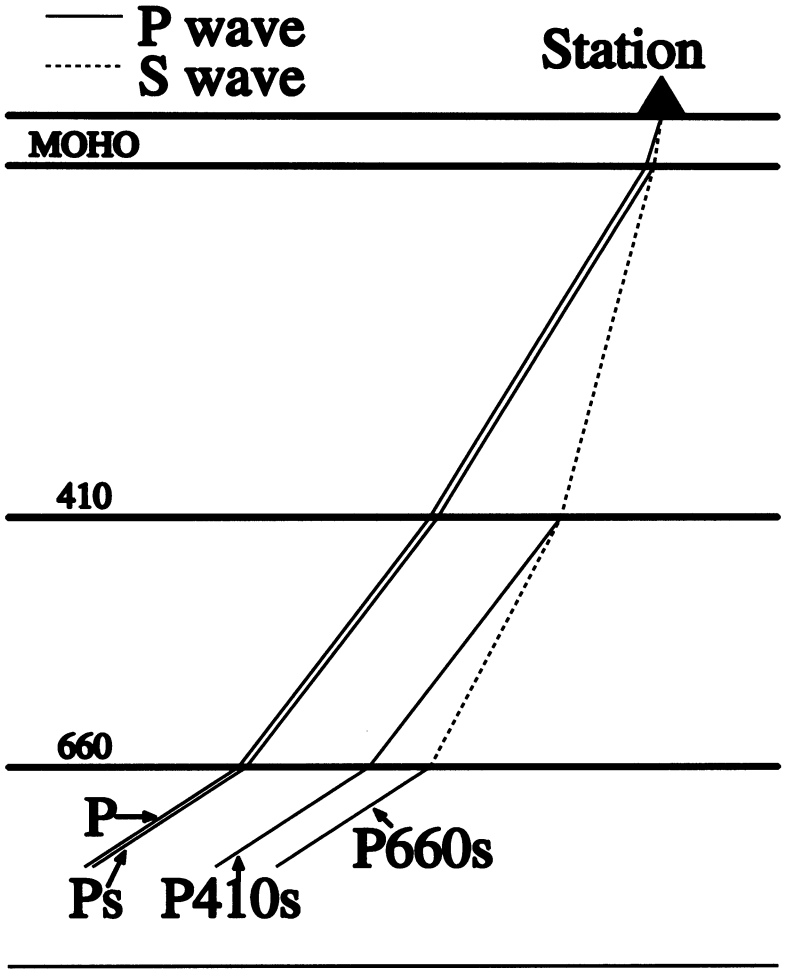

Figure 3.2 Cartoon presents how to generate the Pds phases. When seismic waves meet each discontinuity on the propagation paths, the part energy of direct P wave (solid line) is converted into SV type (dashed line), arriving after the main P wave with a weak amplitude signal (Andrews and Deuss, 2008).

contained largely on the horizontal components. The amplitude, arrival time, and polarity of the locally generated Ps phases are sensitive to the S-velocity structure beneath the recording station. By calculating the time difference in arrival of the converted Ps phase relative to the direct P wave, the depth of the discontinuity can be estimated using a reference velocity model. To obtain the P receiver function, the following steps are generally used in this research.

3.1 Rotation

Niu and Li (2010) found a significant portion of the CEArray stations had problems in orientation. I used their estimates of component azimuth, which were determined from P-wave particle motions, to correct the NS and EW components (Figure 3.1). I applied the two coordinate systems, Langston-Owens and Vinnik-Kosarev (Vinnik, 1977, Kosarev et al, 1993) (Figure 3.3) to rotate the two horizontal components of the seismograms to the radial and transverse components and further to project the two components to the principal directions (longitudinal and in-plane transverse) computed from the covariance matrix (Figure 3.4). The receiver functions were then computed from the data projected into this coordinate system (hereafter referred as to P- and SV-component) (Figure 3.5) (Vinnik, 1977; Niu and Kawakatsu, 1998; Niu et al, 2005).

3.2 Deconvolution

I employed the "water-level" deconvolution technique (Clayton and Wiggins, 1976) to generate receiver functions:

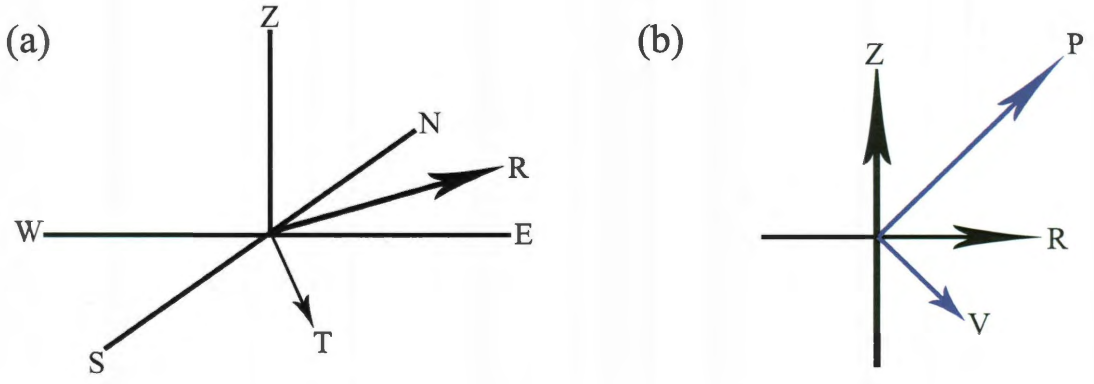

Figure 3.3 Two coordinate systems, Langston-Owens (a) and Vinnik-Kosarev (b) (Vinnik, 1977, Kosarev et al, 1993). I first rotated the two horizontal components of the seismograms to the radial and transverse components and further to project the two components to the principal directions.

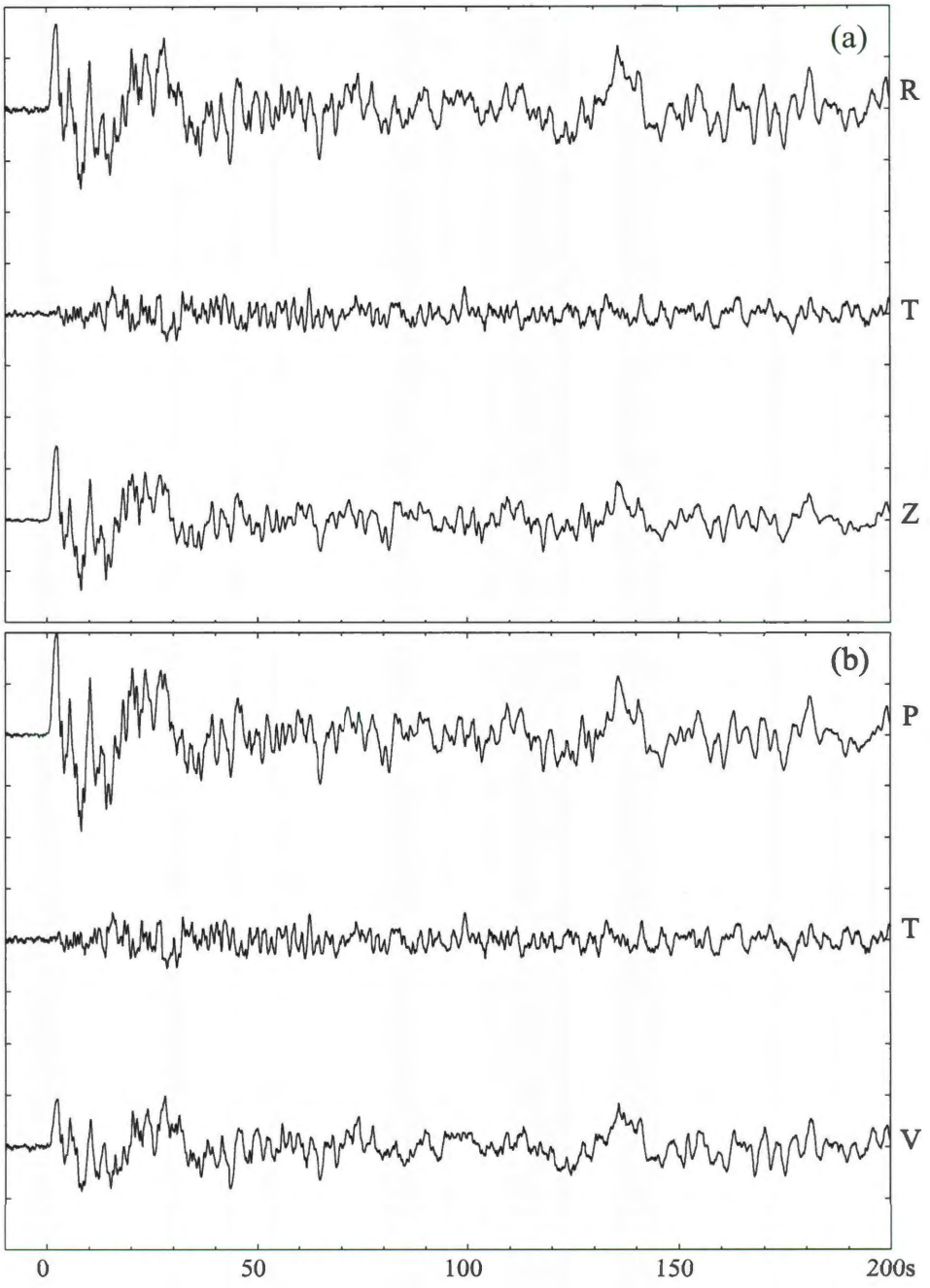

Figure 3.4 (a) Demonstrating the radial and transverse components seismograms generated from NS and EW components. (b) Showing longitudinal and in-plane transverse waves rotated from R and Z.

$$RF(\omega) = \frac{V(\omega) \cdot P^{*}(\omega)}{\max\{|P(\omega)|^2,\ k \cdot |P_{\max}(\omega)|^2\}} e^{-(\frac{\omega}{2a})^2} \tag{3.1}$$

Here *k* and *a* are two constants that define "water level" and the corner frequency of the Gaussian low pass filter. a was set 1.5 in this study, equivalent to a corner frequency of 0.5 Hz. *P(w)* and *V(w)* are the spectra of the P and SV components. I used a 200 s time window (15 s and 185 s before and after the P wave) to compute the source spectrum of each earthquake. I further screened receiver functions with various methods (Chen et al, 2010) to eliminate noisy data. The total number of receiver functions used in the CCP imaging is 37427.

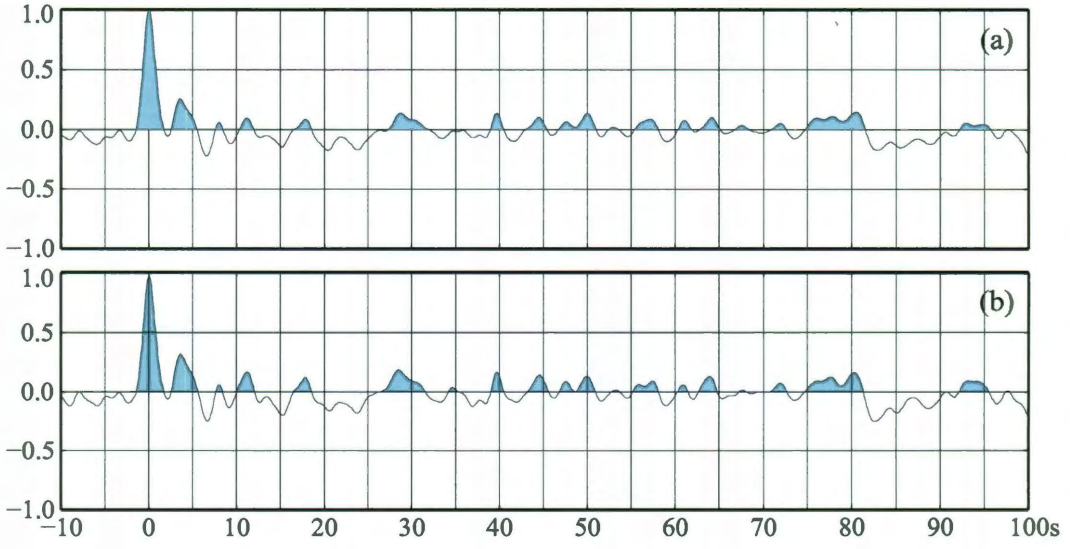

Figure 3.5 Presenting two receiver function examples calculated using radial and vertical components (a), and longitudinal and in-plane transverse waves (b) separately. Two receiver functions have inherent relation and should be similar.

3.3 CCP gathering

I applied the common-conversion-point (CCP) stacking technique to the receiver-function data to image the P to S conversion events and their lateral variations beneath the array (e.g., Dueker and Sheehan, 1997; Niu et al, 2005). For an assumed conversion depth, *d*, I first computed the relative arrival time of the converted phase *Pds* with respect to the direct arrival by ray tracing the two phases using the 1D iasp91 velocity model (Kennett and Engdahl, 1991). I also kept the geographic location of the conversion points and gathered the receiver functions that share the same conversion points. I divided the study area into meshed grids of 0.1° by 0.1°, and used a circular cap with a radius of 1 degree for gathering the receiver functions. This serves to low-pass filter the topographic relief on the two discontinuities with a corner wavelength roughly equivalent to the size of the caps, approximately 200 km. I then summed all the receiver functions within a 0.1 s window centered on the arrival time of *Pds* using an N^{th}-root stacking technique (Muirhead, 1968). For the i^{th} cap, let $r_k(t)$ represents the k^{th} receiver function gathered in the cap, and t_{dk} is the *Pds* arrival time for a discontinuity with a depth of *d*, an N^{th}-root stack, *R(d)*, is given by

$$R_i(d) = y_i(d)\left|y_i(d)\right|^{N-1} \tag{3.2}$$

where

$$y_i(d) = \frac{1}{K}\sum_{k=1}^{K} w_k sign(r_k(\tau_{dk}))\,|\,r_k(\tau_{dk})\,|^{1/N} \tag{3.3}$$

Here K is the total number of receiver functions gathered at the i[th] cap. w_k is a Gaussian weight function

$$w_k = \exp\{-x_k^2 / a^2\} / \sum_{n=1}^{K} \exp\{-x_n^2 / a^2\}. \quad (3.4)$$

Here x_k is the distance between the cap center and the conversion point of the k^{th} event. The Gaussian width parameter, a, was set to be the same as the cap radius. I chose $N=4$ to reduce the uncorrelated noise relative to the usual linear stack ($N=1$), recognizing that this suppresses conversions with significant dip away from the horizontal. I varied d from 300 to 800 km in increments of 1 km. The depth stacked receiver functions along latitude 35ºN and longitude 120ºE are shown in Figure 3.6 (a), 3.7 (a), 3.6 (b) and 3.7(b), respectively. Figure 3.6 and Figure 3.7 show that CCP stacking is an effective method to improve receiver function quality (compared with Figure 3.5). The stacking cross-sections can be easily to identify 410-km and 660-km depths. 4[th] root stack method enhances the 410-km and 660-km signal and suppresses the uncorrelated noise.

3.4 Travel Time Correction

To better image the absolute depths of the two discontinuities, I further used a 3D crustal model derived from *Pn* travel times (Sun and Toksoz, 2006) to correct anomalies on the relative Ps travel time. The crustal model has a 4-layer crust (sedimentary, upper, middle and lower crust) with a horizontal resolution of 1°×1°. I also used the whole mantle P (Fukao et al, 2001) and S-wave velocity models (Grand,

2002) to calculate travel-time anomalies resulting from heterogeneities in the mantle. It seems that both the crustal and mantle corrections are rather minor. The gathered receiver functions based on 3D time move-outs are shown in Figure 3.6 and 3.7, respectively. Compared Figure 3.7 (a) and 3.7 (c), the depth of the two discontinuities changes by less than 5 km.

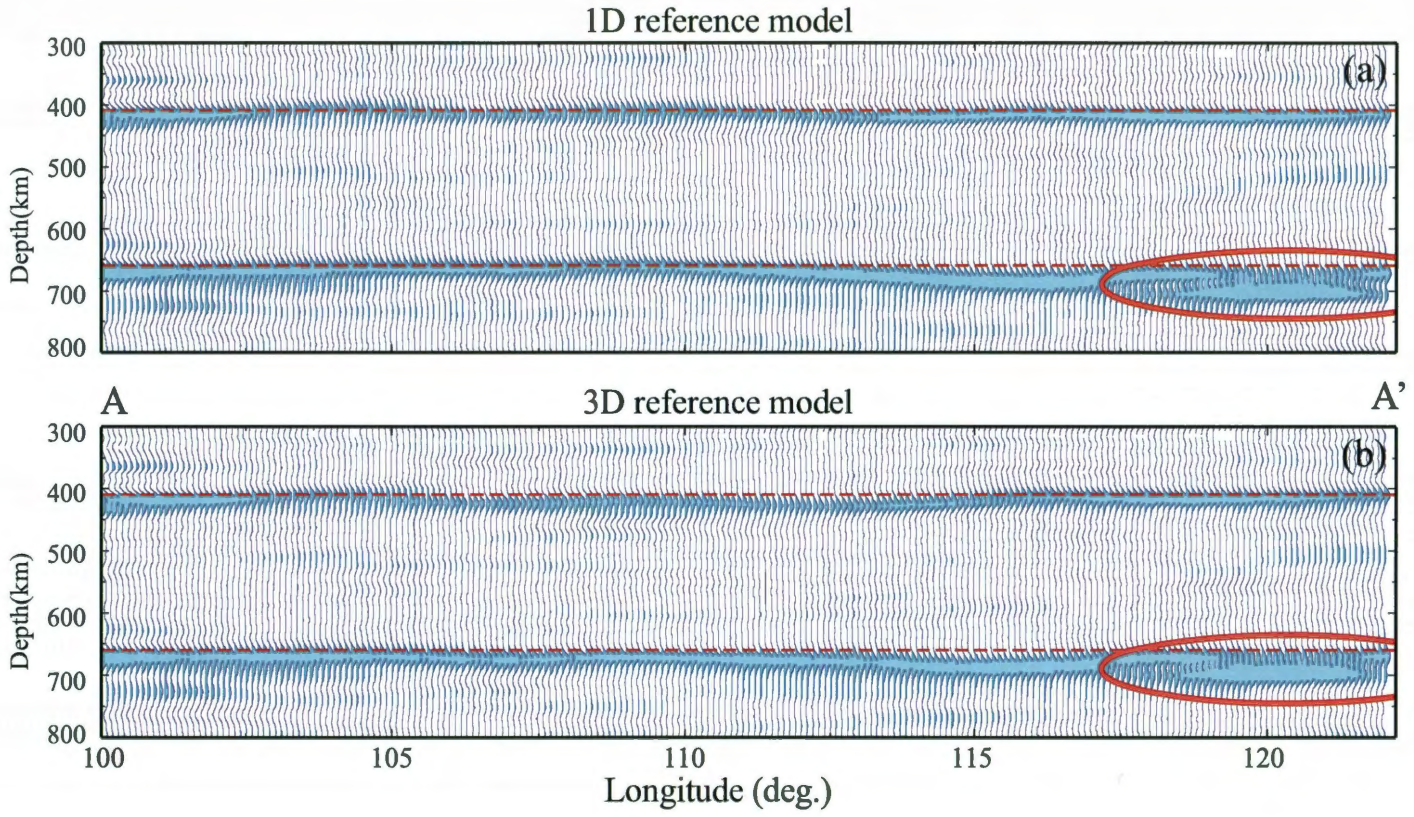

Figure 3.6 3D CCP stacking results were generated with 1th root stacking. (AA') Depth sections of the CCP gathered receiver functions along latitude 35?N computed from a 1D (a) and 3D (b) reference velocity model. (c) and (d) are similar to (a) and (b) except for along longitude 120?E. The locations of two sections are shown in Figure 2.2. Note the clear P to S conversion from the 410 km and 660 km discontinuities. Ellipses indicate the regions with a double branched 660 km discontinuity.

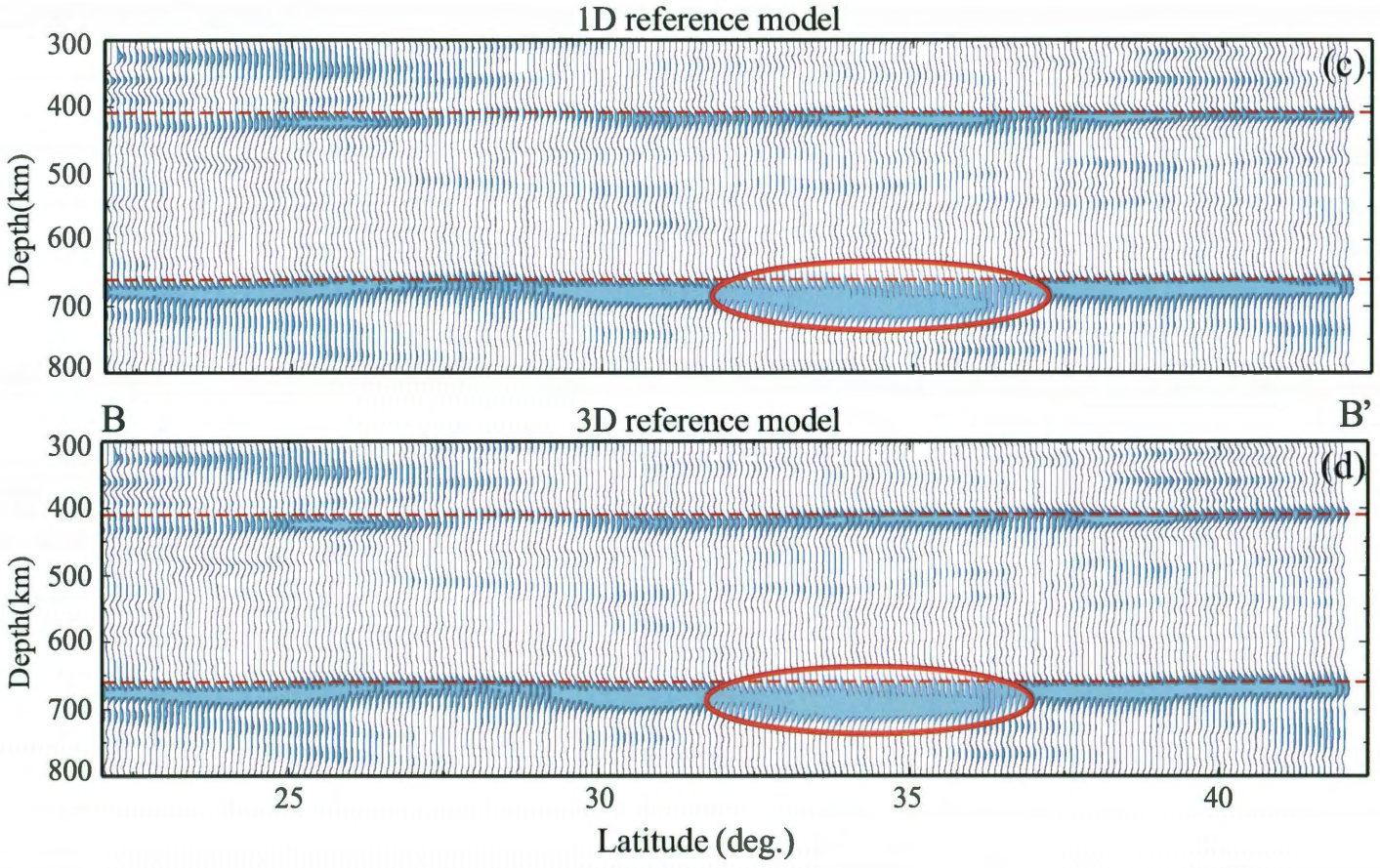
1D reference model
(c)
Depth(km)
300
400
500
600
700
800
B
3D reference model
B'
(d)
Depth(km)
300
400
500
600
700
800
25
30
35
40
Latitude (deg.)

Figure 3.6(BB')

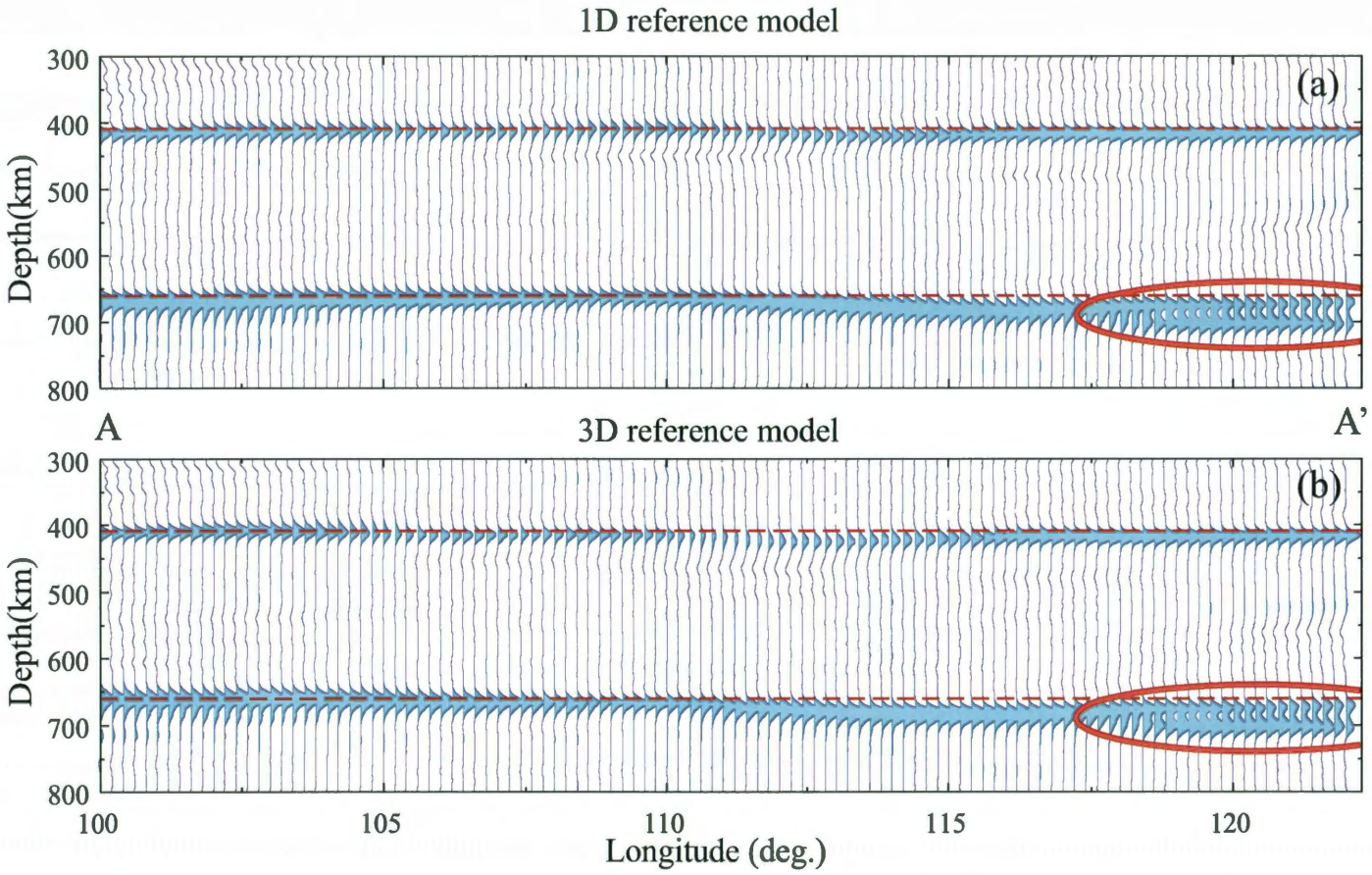

Figure 3.7 3D CCP stacking results were calculated with 4th root stacking method. Other labels are same as Figure 3.6. 4th root stacking method enhances signal quality. Figure 3.7 have the same characters as Figure 3.6, except the uncorrelated noise is suppressed.

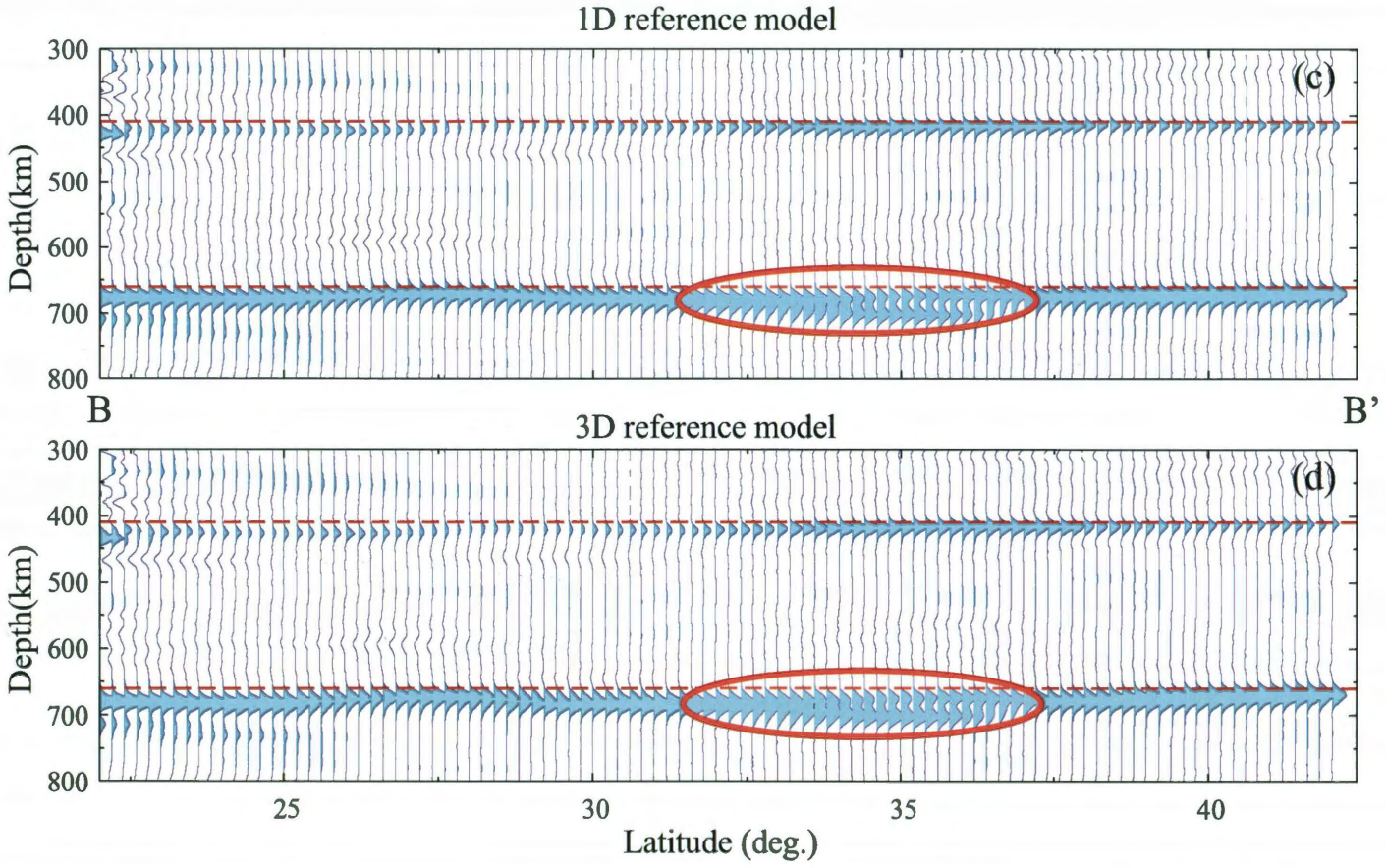
1D reference model
(c)
Depth(km)
300
400
500
600
700
800
B
B'
3D reference model
(d)
Depth(km)
300
400
500
600
700
800
25
30
35
40
Latitude (deg.)

Figure 3.7(BB')

Chapter 4

Results and Discussion

As shown in Figure 3.7, both the 410-km and 660-km discontinuities can be identified easily from the two depth sections. I manually picked the two discontinuities from all the stacked receiver functions. The average depth of the 410-km and the 660-km is 418.2 km and 673.7 km, respectively. The 410-km is roughly similar to the global average (418 km) while the 660-km is about 14 km deeper than the global average (660 km) obtained from SS precursor studies (Flanagan and Shearer, 1998; Gu and Dziewonski, 2002). Consequently the transition zone thickness is 255.5 km, 13.5 km thicker than the global average. Gu and Dziewonski (2002) found that in general continents are underlain by a thicker transition zone than oceans, and the transition zone beneath the Eurasian plate is ~9 km thicker than the global average. The observed thick transition zone here thus is consistent with theirs and may indicate that the average temperature within the transition zone is lower here due to a rather complicated subduction history

including the subuction of the Pacific plate since Jurassic.

The lateral variation of the 410-km relief is shown in Figure 4.1(a) with the counts of the Ps conversion points in each cap (Figure 4.1(b)). The discontinuity beneath the west side of the NSGL (413.9 km) appears to be significantly shallower than the east side (421.9 km). This difference is unlikely related to the presence of the subducted Pacific slab which penetrates the 410-km at a location further east to the study region (Fukao et al, 2001; Huang and Zhao, 2006; Li and van der Hilst 2010). Rather it is likely that the east-west contrast observed here is caused by unmodeled velocity structure in the upper mantle. Li and van der Hilst (2010) found that the lithosphere beneath the Precambrian Ordos and Sichuan basins has substantially high seismic velocities and the high velocity regions extend to at least 250 km deep. The 410-km beneath the two basins are ~10 km shallower than the surrounding areas, suggesting the shoaling of the 410-km is rather an artifact of the reference model. I note that the uplift shown at the upper left corner of the map (labeled as UL in Figure 4.1(a)) is not robust since I have almost no data coverage in this region. The most prominent feature the 410-km relief map shown in Figure 4.1 is a ~15 km depression beneath the Quaternary Datong volcano located at the northeastern edge of the Ordos plateau in north China. Interpreting this depression will be combined with transition-zone thickness in the later part of the discussion.

As shown in Figure 3.7, the 660-km beneath the Yellow sea south of the Shandong peninsula appears to have two branches. I picked the depth of the two branches and the lateral variations based on these picks are shown in Figure 4.2(a)

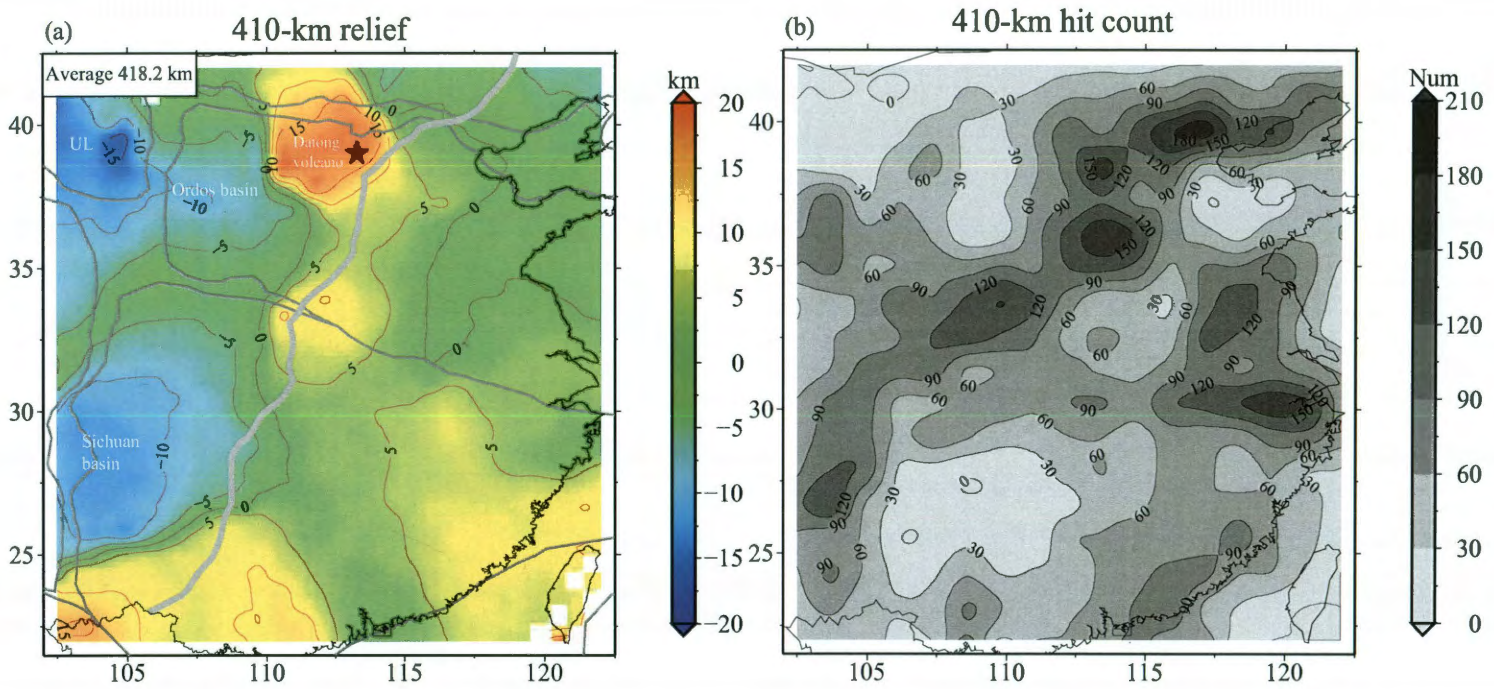

Figure 4.1 (a) Map showing the depth variations of the 410 km discontinuity. Note that the average depth was removed from the depth. The thick grey line indicates the North South Gravity Lineament. The thin grey lines show the boundaries of the major tectonic blocks in the study region. (b) Number of receiver functions gathered at each grid point for stacking. Note that due to the number of events recorded at each station varies significantly, so the conversion density map shown here is slightly different from the station distribution map shown in Figures 2.1 and 2.2.

and 4.2 (b), respectively. Chen and Ai (2009) also found a double-branched 660-km roughly in the same areas. Beside the double 660-km, I also observed an east-west contrast in the depth of the discontinuity. The region located at the west side of the NSGL has a shallower 660-km (666.9 km) than the east side (680.2 km) does. As discussed in the last paragraph, part of this contrast is likely to result from unmodeled 3D velocity heterogeneities. The NSGL seems to well coincide with the western edge of the area with a significantly depressed 660-km. Huang and Zhao (2006) found that the western front of the subhorizontally lying Pacific plate inside the transition zone is spatially consistent with the NSGL. They suggested that the subducting Pacific plate might have significant influence on surface topography. Chen and Ai (2009) also found the same correlation from the transition-zone thickness map beneath north China.

The mantle transition-zone thickness computed from the depths of the two disconstinuities is shown in Figure 4.3 (a). Here I removed the mean value to show lateral variations of the transition-zone thickness. I found a thickened transition zone around the western Yellow sea where a double-branched 660-km is observed. Li and van der Hilst (2010) found a NNE trending high velocity anomaly (TZ2 in their Figure 2(4)) beneath the Bohai and Yellow sea between 30°N and 40°N. They interpreted it as the subducted Pacific plate during late Cretaceous and Paleogene (Figure 4.3(b)). The anomalous region on our transition-zone thickness map is located between 30°N and 37°N. I have many data that sample the Bohai Sea region, so the northern edge of the anomaly should be well constrained. However, if the transition zone beneath the Bohai Sea has a low Vp/Vs ratio in addition to the high

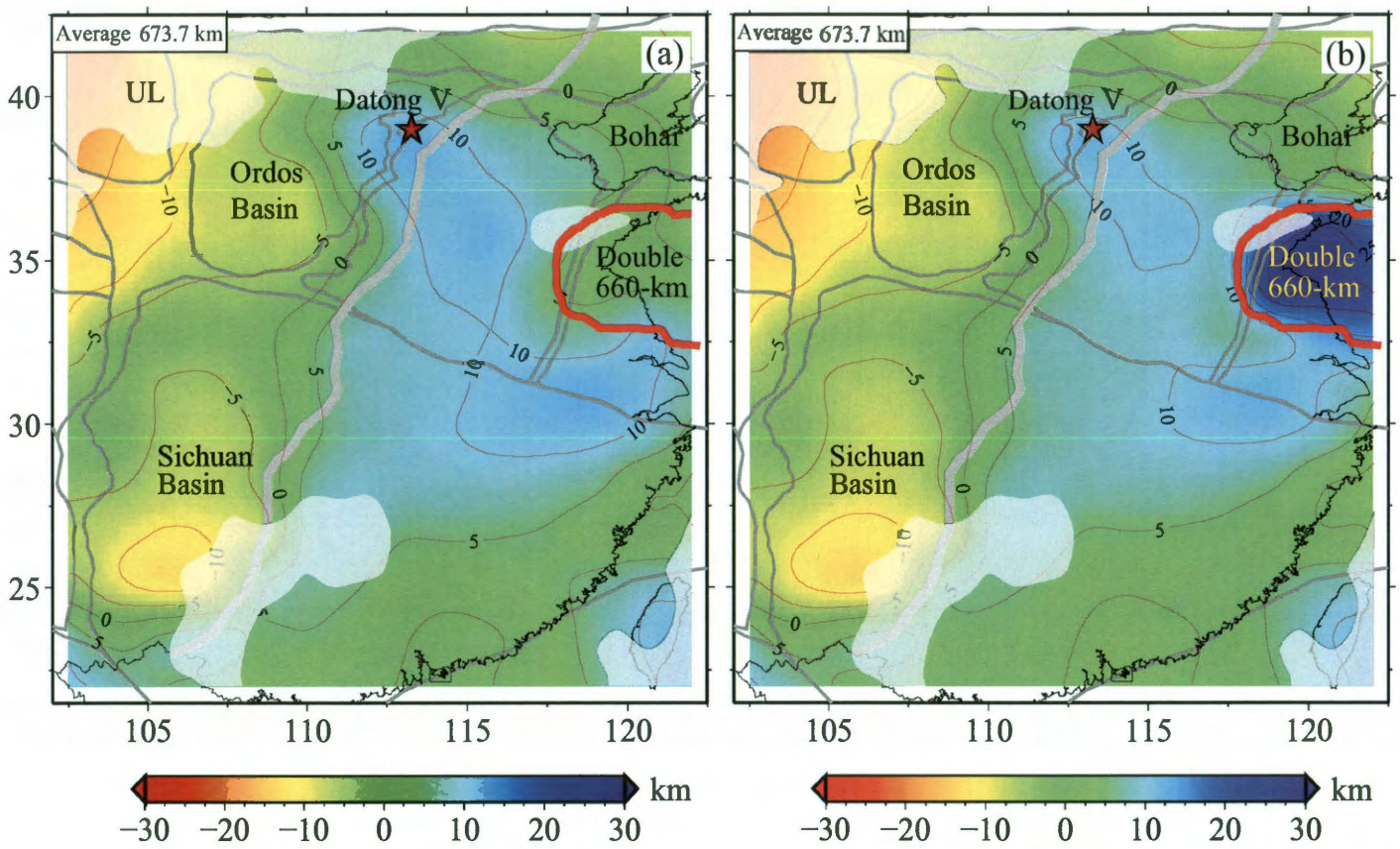

Figure 4.2, Map view of the depth variations of the 660 km discontinuity picked from the deep (a) and the shallow branch (b) of the 660 km discontinuity. Light shades indicate regions with only a few receiver functions (<30) that can be used for stacking. Consequently, the results shown in these regions may not be robust. The solid red line outlines the region with a two branched 660 km discontinuity. The thin and thick grey lines represent tectonic block boundaries and the North South Gravity Lineament, respectively.

P-wave velocity, then the transition zone can be significantly (> 5 km) underestimated.

The western front of the anomaly is located at ~115°E, two to three hundreds kilometers east to the NSGL. The good correlation observed between the surface topography and the depth of the 660-km is absent here. Since estimates of transition zone thickness are less influenced by 3D velocity structure above the 410-km discontinuity, the transition zone thickness has been considered as a better thermometer of the transition zone compared to the absolute depth estimates of the two discontinuities. Thus I tend to argue that the correlation between surface topography and the transition zone structure proposed by previous studies is questionable and requires further quantitative investigation. It also seems that this correlation is not shown in the tomographic images of Li and van der Hilst (2010). As I discussed above, the transition thickness map shown here still suffers from unmodeled velocity heterogeneities in the transition zone, it is hard to make a definitive argument whether the surface topography is controlled by the subducted Pacific slab. Both the India-Asia collision and the eastward retreat of the Pacific subduction could play a role in determining the boundary between the compressional and extensional terranes.

Although the 410-km beneath the Datong volcano shows a prominent ~15 km depression, the transition zone thickness beneath the volcano appears to be rather normal (Figure. 4.3). While a normal transition zone implies that the origin of the observed volcanism is likely within the upper mantle, the depth extent of the

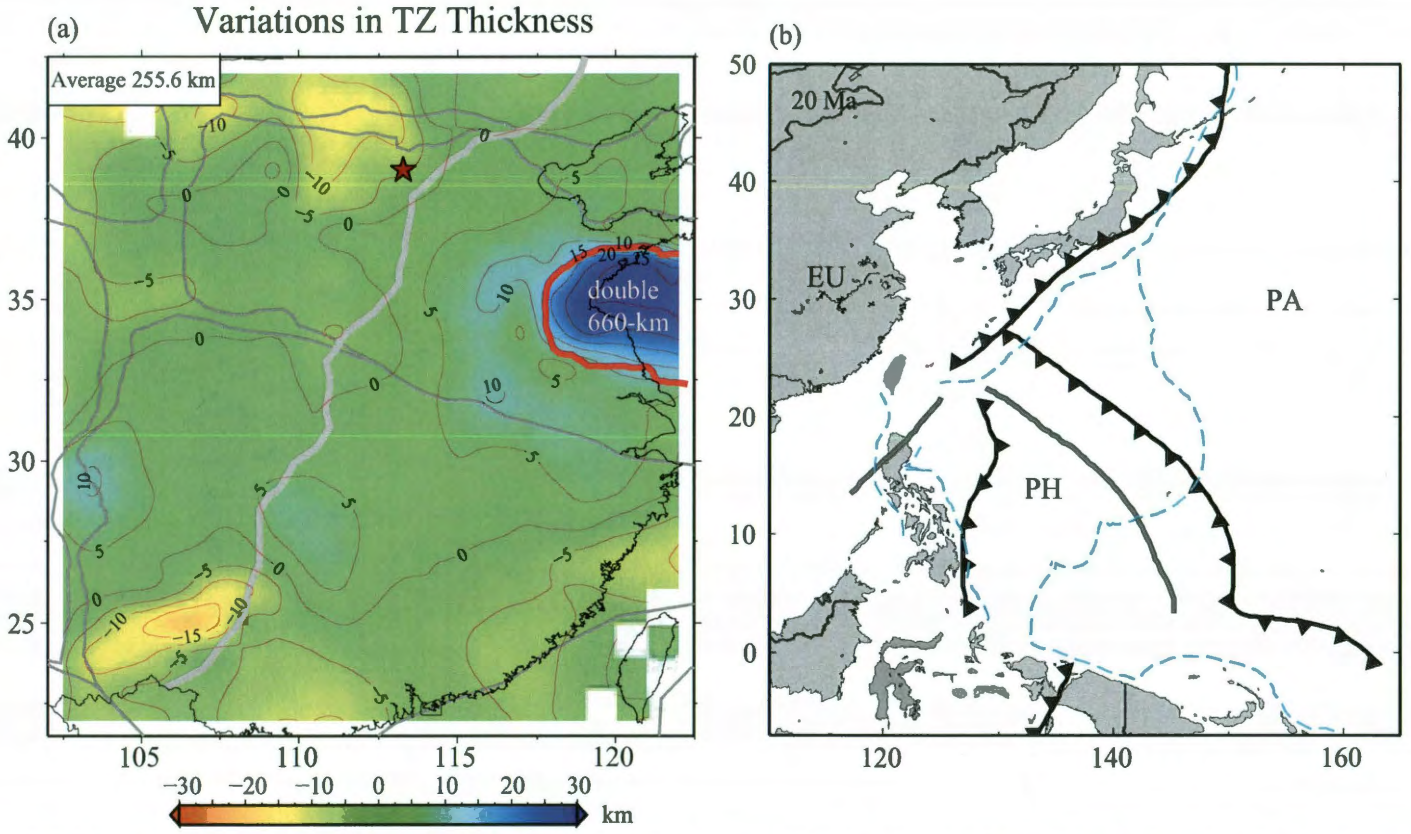

Figure 4.3 (a) Map showing the thickness variations of the transition zone. In the region where a double branched 660 km is observed, depths of the deep branch of the 660 km discontinuity were used in computing transition zone thickness. (b) Map showing the subducting Pacific plate along the east coast and southwest Japan at late Oligocene (Hall, 2002), currently being replaced by the subducting Philippine plate due to the opening of the Philippine Sea. Black lines with solid triangles indicate the trench locations ~20 Ma ago. Cyan dash lines show the current plate boundaries, and solid gray lines illustrate active spreading centers.

upwelling associated with the volcanism is not well constrained here. Based on the observed ~15 km depression on the 410-km, I estimated the amount of velocity anomalies in the upper mantle. If the depression is caused by an unmodeled low velocity anomaly in the upper mantle, it requires either a strong (4-8%) localized low velocity anomaly near the lithosphere-asthenosphere boundary or ~1.5% low velocity column across the entire upper mantle above the 410-km. The later is more consistent with the results from recent tomographic study of Li and van der Hilst (2010), who found a prominent low-velocity anomaly extending to almost 400 km beneath the Datong volcano.

Xu et al (2005) analyzed the geochemical and isotopic compositions of alkali and tholeiitic basalts collected from the Datong volcanic field. They found that the alkali basalts have relatively homogeneous geochemical and isotopic compositions similar to oceanic island basalts. Thus the alkali basalts are likely derived from asthenosphere. The tholeiitic basalts appear to be originated near the lithosphere-asthenosphere boundary, which is located ~50-70 km deep below surface. Based on the geographic distribution of the alkali and tholeiitic basalts, which were found progressively from northwest to southeast, they suggested the lithosphere beneath the volcanic field thins progressively from northwest to southeast before it deeps drastically beneath the Taihangshan mountain range. The rapid change in the depth of the lithosphere-asthenosphere boundary induces a secondary convection, the so-called edge driven convection, and results in a small-scale upwelling responsible for the observed volcanism. The scenario thus suggests a shallow origin near the lithosphere-asthenosphere boundary for the volcanism occurred at Datong if the

lateral scale of the convection is limited in local scale. Thus further seismic studies are needed to provide better images under the volcano.

Observation of multiple velocity jumps at depths between 650 and 750 km have been reported by many studies. Niu and Kawakatsu (1996) found a complicated 660-km at the tip of the subducting Pacific plate beneath northeastern China. They interpreted the observed triple velocity jumps to result from garnet transformations together with the post-spinel phase transition. Ai et al (2003) confirmed the presence of this multiple-discontinuity structure in a broader area beneath northeastern China. They also found the regions with multiple seismic discontinuities are intermittently distributed, and are mixed with regions with a simple depressed 660-km discontinuity, which suggests that the phase diagrams of the non-olivine minerals are extremely sensitive to temperature, as shown in the calculation of Vacher et al (1998). Simmons and Gurrola (2000) found multiple seismic discontinuities near the base of the transition zone beneath southern California, where there is no subducting slabs. Hirose et al (1999) found that the post-garnet transformation starts at 26 GPa (equivalent to a depth of 720 km) and 2,000 K and completes within a 1 GPa interval. Simmons and Gurrola (2000) employed this phase change to interpret their observation. A 2000 K at ~700 km depth implies a 1650 K adiabat, which is slightly high than the regular mantle potential temperature of 1550 K proposed by McKenzie and Bickle (1988). A slightly elevated temperature agrees with the low seismic velocities observed beneath southern California.

The double-branched 660-km is not observed along the entire strike of the Cretaceous-Paleogene Pacific slab, rather it is found only in a narrow area with an NS extension of ~350 km (Figure 4.3). I noticed that this multiple-branch feature is not shown at the 410 km discontinuity (Figure 3.7). In addition, this feature is always shown in the CCP images regardless of whether a 1D or 3D reference model is used. Thus I believe it is a robust feature reflecting the nature of the 660-km in the area rather than a numerical artifact. The double-branched 660-km region observed here, on the other hand, is much smaller than those observed by Gao et al (2010) with the National Seismograph Network of China (NSNC). Single station stacking method was used in their study. In principle, as the conversion points at the 660-km spread in a quite large area (~2.5 degree in radius), the single-station stacking method has the risk of mapping depth variations of a discontinuity into multiple ones. This could be one possible explanation of the observed discrepancy, although more careful comparison of the two methods with a similar dataset is needed in order to clear this issue.

Temperature plays a key role in determining the phase diagram of garnet. It has been shown that at very lower temperature condition (1000 K adiabat) garnet dissolves into ilmenite at around 620 km and stays stable down to 710 km depth when it starts to transform into perovskite (Vacher et al, 1998). These phase changes together with the post-spinel reaction of the olivine produce a multiple jumps in seismic velocity. As temperature increases, the stable depth range of ilmenite decreases drastically. At a regular mantle adiabat (~1550 K), the garnet dissolves into perovskite directly at roughly the same depth of the post-spinel phase

transition, which leads to a single and enhanced velocity jump. At higher temperature, the post-garnet phase transition requires a higher pressure than the post-spinel reaction does. The post-garnet transformation completes in a 30-50 km depth range (Hirose et al, 1999; Akaogi et al, 2002; Vitos et al, 2006), implying a second velocity jump below the main 660-km caused by the post-spinel phase change.

The observed lateral distribution of the double-branched 660-km thus provides strong constraints on the lateral variation in temperature at the base of the transition zone. Based on the three scenarios discussed above, the double-branched 660-km region is likely to have a very low temperature, cold enough to allow ilmenite to be stable. The remaining slab, being continuously warmed for millions of years, is not cold enough to allow a stable ilmenite to exist. Instead, garnet transforms directly into perovskite, and this transformation occurs at roughly the same depths where ringwoodite dissolves into perovskite plus magnesiowustite. The temperature of the remaining slab is, however, still significant low (~100 K) compared to its surrounding regions, resulting in a depressed 660-km. In general temperature at the base of the transition zone in our study area is not high enough to promote a prominent post-garnet phase transition at a great depth. Thus I don't see any multiple-branched 660-km, like those observed in southern California (Simmons and Gurrola, 2000) outside the Cretaceous-Paleogene Pacific slab. The observed lateral variation in temperature within the subducted slab could also be related to the temporal-spatial evolution history of the subduction along the east coast of China (Figure 4.3(b)). Due to the northeastward retreat of the Izu-Bonin-

Mariana trench, the subduction along the east coast of China was closed progressively from south to north, resulting in an increase in the volume of subducted slab toward the north. This may explain why the northern section of the slab is colder than its southern neighbor. This is another possible interpretation for the limited distribution of the double-branched 660-km observed here, which is related to the subduction geometry. It is conceivable that the post-garnet phase transition needs to occur in a broad area in order to be imaged by a relatively low-frequency dataset used in this study.

I investigated the mantle transition-zone structure beneath eastern and central China using a large amount of waveform data recorded at the national and region seismic networks of the China Earthquake Administration. The CCP images from receiver function data showed the following features the 410-km and 660-km discontinuity beneath the study region: (1) Although there is good correlation between the surface topography and the estimated depths of the two discontinuities, the western front of the subducting Pacific plate doesn't seem to be obviously correlated with the topographic boundary between eastern and western China, suggesting that the Pacific subduction is not necessarily the sole process in controlling the western extent of the eastern terrane of China; (2) The Quaternary Datong volcano is underlain by a localized low velocity anomaly that may extend to ~400 km below the surface; (3) The presence of the Pacific plate subducted during the late Cretaceous and Paleogene is manifested by a double-branched 660-km discontinuity located beneath the Yellow sea and surrounding regions with a moderately depressed 660-km.

References

Ai Y S, Zheng T Y, Xu W W, He Y M and Dong D (2003). A complex 660km discontinuity beneath northeast China. *Earth Planet Sci Lett* **212:** 63-67.

Ai Y, Chen Q, Zeng F, Hong X and Ye W (2007). The crust and upper mantle structure beneath southeastern China. *Earth and Planetary Science Letters* **260**: 549-563.

Akaogi M, Tanaka A and Ito E (2002). Garnet–ilmenite–perovskite transitions in the system Mg4Si4O12–Mg3Al2Si3O12 at high pressures and high temperatures: phase equilibria, calorimetry and implications for mantle structure. *Phys Earth Planet Sci Int* **132:** 303-324.

Anderson, D (1989), Theory of the Earth, *Blackwell Scientific Publications* 366 pp.

Benoît Tauzin, Eric Debayle and GérardWittlinger. (2010). Seismic evidence for a global low-velocity layer within the Earth's upper mantle, *nature geoscience*

Bercovici D, Karato S-I. (2003). Whole-mantle convection and the transition-zone water filter. *Nature* **425**:39–44

Bolfan-Casanova N, Mackwell S, Keppler H, McCammon C, Rubie DC. (2002). Pressure dependence of H solubility in magnesiow¨ ustite up to 25 GPa: implications for the storage of water in the Earth's lower mantle. *Geophys. Res. Lett.* **29(10):**1029–32.

Chen L and Ai Y. (2009). Discontinuity structure of the mantle transition zone beneath the North China Craton from receiver function migration. *J Geophys Res* **114**: 1-16.

Chen Y L, Niu F L, Liu R F, Huang Z B, Tkalcic H, Sun L and Winston C (2010). Crustal structure beneath China from receiver function analysis. *J Geophys Res* **115**: 1-22.

Clayton R A and Wiggins R W (1976). Source shape estimation and deconvolution of teleseismic body waves. *Geophys J R Astron Soc* **47**: 151–177.

Deuss, A. (2007) Seismic observations of transition zone discontinuities beneath hotspot locations. *Special Papers of the Geological Society of America*, 430. pp. 121-136.

Dueker K G and Sheehan A F (1997). Mantle discontinuity structure from midpoint stacks of converted P and S waves across the Yellowstone hotspot track. *J Geophys Res* **102**: 8313-8328.

Engebretson, D. C., K. P. Kelley, H. J. Cashman, and M.A. Richards. (1992). 180 million years of subduction *GSA Today*, **2**,93-100.

Fee, D., and K. Dueker. (2004). Mantle transition zone topography and structure beneath the Yellowstone hotspot, *Geophys. Res. Lett.*, 31, L18603, doi:10.1029/2004GL020636.

Flanagan M and Shearer P (1998). Global mapping of topography on transition zone velocity discontinuities by stacking SS precursors. *J Geophys Res* **103:** 2673-2692.

Fukao Y, Obayashi M, Nakakuki T and the Deep Slab Project Group (2009). Stagnant Slab: A Review. *Annual Review of Earth and Planetary Sciences* **37**: 19-46.

Fukao Y, Widiyantoro S and Obayashi M (2001). Stagnant slabs in the upper and lower mantle transition region. *Rev Geophys* **39**: 291-323.

Gao Y, Suetsugu D, Fukao Y, Obayashi M, Shi Y, Liu R (2010), Seismic discontinuities in the mantle transition zone and at the top of the lower mantle beneath eastern China and Korea: Influence of the stagnant Pacific slab. *Phys Earth Planet Inter* **183**: 288-295.

Gao, W., E. Matzel, and S. P. Grand. (2006). Upper mantle seismic structure beneath eastern Mexico determined from P and S waveform inversion and its implications, *J. Geophys.Res.*, 111, B08307, doi:10.1029/2006JB004304.

Giardini, D. and Woodhouse, J. H. (1984) *Deep seismicity and modes of deformation in Tonga subduction zone Nature* **307**, 505–509.

Grand S P (2002). Mantle shear-wave tomography and the fate of subducted slabs. *Phil Trans R Soc A* **360**: 2475–2491.

Grand, S. P., (1994), Mantle shear structure beneath the Americas and surrounding oceans: *Journal of Geophysical Research*, v. **99**, p. 11591–11621.

Gu Y J, and Dziewonski A M (2002). Global variability of transition zone thickness. *J Geophys Res* **107** (B7): 1-20.

Gudmundsson, O. and Sambridge, M. (1998). A regionalized upper mantle (RUM) seismic model. *J. Geophys. Res.*, **103**:7121-7136.

Hall R (2002). Cenozoic geological and plate tectonic evolution of SE Asia and the SW Pacific: computer-based reconstructions, model, and animations. *J Asian Earth Sci* **20:** 353-431.

Hirose K, Fei Y W, Ma Y Z and Mao H K(1999). The fate of subducted basaltic crust in the Earth's lower mantle. *Nature* **397:** 53-56.

Hirschmann M (2006). Water, Melting, and the deep Earth H2O Cycle. *Annual Review of Earth and Planetary Sciences* **37**: 19-46.

Huang J L and Zhao D P (2006). High-resolution mantle tomography of China and surrounding regions. *J Geophys Res* **111** (B09305): 1-21.

Huang J P, Vanacore E, Niu F L and Levander A (2010). Mantle transition zone beneath the Caribbean-South American plate boundary and its tectonic implications. *Earth Planet Sci Lett* **289:** 105-111.

Inoue T, Yurimoto H and Kudoh Y (1995). Hydrous modified spinel, Mg1.75SiH0.5O4: a new water reservoir in the mantle transition region. *Geophys. Res. Lett.* **22**: 117- 20.

Ito E and Takahashi E (1989). Postspinel transformations in the system Mg_2SiO_4-Fe_2SiO_4 and some geophysical implications. *J Geophys Res* **94**: 10637-10646.

Jasbinsek, J. J., K. G. Dueker, and S. M. Hansen. (2010). Characterizing the 410 km discontinuity low velocity layer beneath the LA RISTRA array in the North American Southwest, *Geochem. Geophys. Geosyst.*, 11, Q03008, doi:10.1029/2009GC002836.

Jasbinsek, J., and K. G. Dueker. (2007). Ubiquitous low velocity layer atop the 410!km discontinuity in the northern Rocky Mountains, *Geochem. Geophys. Geosyst.,* 8, Q10004,doi:10.1029/2007GC001661.

Katsura T and Ito E (1989). The system Mg_2SiO_4-Fe_2SiO_4 at high pressures and temperatures: precise determination of stabilities of olivine, modified spinel and spinel. *J Geophys Res* **94**: 15663-15670.

Kawamoto T, Hervig RL, Holloway JR. 1996. Experimental evidence for a hydrous transition zone in the early Earth's mantle. *Earth Planet. Sci. Lett.* **142**: 587–92.

Kennett B N and Engdahl E R (1991). Travel times for global earthquake location and phase identification. *Geophys J Int* **105**: 429-465.

Koga K, Hauri E, Hirschmann MM and Bell D (2003). Hydrogen concentration analyses using SIMS and FTIR: comparison and calibration for nominally anhydrous minerals. *Geochem. Geophys. Geosyst.* 4:1019, doi:10.29/2002GC000378.

Kohlstedt DL, Keppler H, Rubie DC. (1996). Solubility of water in the phases of (Mg,Fe)2SiO4. *Contrib. Mineral. Petrol.* **123**: 345–57.

Li C and Van der Hilst R D (2010). Structure of the upper mantle and transition zone beneath Southeast Asia from traveltime tomography. *J Geophys Res* **115**: 1-19.

Li X and Yuan X (2003). Receiver functions in northeast China – implications for slab penetration into the lower mantle in northwest Pacific subduction zone. *Earth and Planetary Science Letters* **226(4):** 679-691.

Li, B., R. C. Liebermann, and D. J. Weidner. (1998). Elastic moduli of waldsleyite (-Mg_2SiO_4) to 7 Gigapasscals and 873 Kelvin, *Science*, **281**: 675-677.

Litasov K, Ohtani E. (2002). Phase relations and melt compositions in CMAS-pyrolite-H2O system up to 25 GPa. *Phys. Earth Planet. Int.* **134**:105–27.

McKenzie D and Bickle M J (1988). The Volume and Composition of Melt Generated by Extension of the Lithosphere. *J Petrology* **29:** 625-679.

Muirhead K J (1968). Eliminating false alarms when detecting seismic events automatically. *Nature* **217**: 533-534.

Niu F L and Kawakatsu H (1996). Complex structure of the mantle discontinuities at the tip of the subducting slab beneath the northeast China: A preliminary investigation of broadband receiver functions. *J Phys Earth* **44:** 701-711.

Niu F L and Kawakatsu H (1998). Determination of the absolute depths of the mantle transition zone discontinuities beneath China: Effect of stagnant slabs on mantle transition zone discontinuities. *Earth Planets and Space* **50**: 965-975.

Niu F L and Li J (2010). Component azimuths of the CEArray stations estimated from P-wave particle motion. *Earthquake Science* **24**: 3-13.

Niu F L, Levander A, Ham S and Obayashi M (2005). Mapping the subducting Pacific slab beneath southwest Japan with Hi-net receiver functions. *Earth Planet Sci Lett* **239**: 9-17.

Niu, F. L., A. Levander, C. M. Cooper, C. A. Lee, A. Lenardic, and D. E. James. (2004). Seismic constraints on the depth and composition of the mantle keel beneath the Kaapvaal craton, *Earth Planet. Sci. Lett.*, **224**: 337– 346.

Obayashi, M., T. Sakurai, and Y. Fukao. (1997). Comparison of recent tomographic models, Abstract of *International Symposium on New Images of the Earth's Interior through Long-term Ocean-floor Observations*, 29.

Revenaugh, J., and S. A. Sipkin. (1994). Seismic evidence for silicate melt atop the 410!km mantle discontinuity, *Nature,* 369(6480), 474–476, doi:10.1038.

Shen X, Zhou H and Kawakatsu H (2008). Mapping the upper mantle discontinuities beneath China with teleseismic receiver functions. *Earth Planets Space* **60**: 713-719.

Simmons N A and Gurrola H (2000). Multiple seismic discontinuities near the base of the transition zone in the Earth's mantle. *Nature* **405:** 559-562.

Song, T. A., D. V. Helmberger, and S. P. Grand. (2004). Low velocity zone atop the 410 seismic discontinuity in the northwestern United States, *Nature*, 427, 530–533, doi:10.1038.

Sun Y S and Toksoz M N (2006). Crustal structure of China and surrounding regions from P wave traveltime tomography. *J Geophys Res* 111 (B03310): 1-12.

Thomas, C., and M. I. Billen (2009), Mantle transition zone structure along a profile in the SW Pacific: Thermal and compositional variations, *Geophys. J. Int.,* 176, 113–125, doi:10.1111 /j.1365-246X.2008.03934.x.

Vacher P, Mocquet A and Sotin C (1998). Computation of seismic profiles from mineral physics: the importance of the nonolivine components for explaining the 660 km depth discontinuity. *Phys Earth Planet Inter* **106:** 275-298.

Van der Hilst, R.D., Widyantoro, S., and Engdahl, E.R. (1997). Evidence for deep mantle circulation from global tomography, *Nature*, v. 386, p. 578-584.

Vinnik L P (1977). Detection of waves converted from P to SV in the mantle. *Phys Earth Planet Inter* **15**: 39–45.

Vinnik, L., and V. Farra (2007), Low S velocity atop the 410!km discontinuity and mantle plumes, *Earth Planet. Sci. Lett.,* 262(3–4), 398–412, doi:10.1016.

Vinnik, L., M. R. Kumar, R. Kind, and V. Farra. (2003). Super deep low velocity layer beneath the Arabian plate, *Geophys. Res. Lett.,* 30(7), 1415, doi:10.1029/ 2002GL016590.

Vitos L, Magyari-Kope B, Ahuja R, Kollar J, Grimvall G and Johansson B (2006). Phase transformations between garnet and perovskite phases in the Earth's mantle: A theoretical study. *Phys Earth Planet Inter* **156:** 108–116.

Wang X and Niu F (2011). Imaging the mantle transition zone beneath eastern and central China with CEArray receiver functions. *Earthquake Science* **24**: 65-75.

Xu Y G, Ma J L, Frey F A, Feigenson M D and Liu J F (2005). Role of lithosphere–asthenosphere interaction in the genesis of Quaternary alkali and tholeiitic basalts from Datong, western North China Craton. *Chem Geol* **224:** 247-271.

Young T E, Green H W, Hofmeister A M, Walker D (1993). Infrared spectroscopic investigation of hydroxyl in β-(Mg, Fe)2SiO4 and coexisting olivine: implications for mantle evolution and dynamics. *Phys. Chem. Miner.* **19**: 409–22.

Zhao D P, Sheng Y and Eiji O (2011). East Asia: Seismotectonics, magmatism and mantle dynamics. *Journal of Asian Earth Sciences* **40(3):** 689-709.

Zheng X F, Ouyang B, Zhang D N, Yao Z X, Liang J H and Zheng J (2009). Technical system construction of Data Backup Centre for China Seismograph Network and the data support to researches on the Wenchuan earthquake. *Chinese J Geophys* (in Chinese) **52**: 1412-1417.